Sex-specific signatures in cardiac anatomy and function in CMR-Derived Biventricular Digital-Twins

Stefano Buoso[*†], Valery L Visser[†], Pia Leuders[†], Maximilian Fuetterer[†], Christina Spengler[$], and Sebastian Kozerke [†]

[†] Institute for Biomedical Engineering, ETH and University of Zurich, Switzerland
[*]corresponding author: e-mail: buoso@biomed.ee.ethz.ch
[$] Department of Health Science and Technology, ETH Zurich, Switzerland

Abstract. Statistical models of cardiac anatomy and motion often pool data across sexes, yet it remains unclear how biological sex differences are represented in these models. When applied to pooled cohorts, linear principal component analysis may capture between-sex variation as dominant modes, potentially complicating the interpretation of anatomical and functional variability. Here, we investigate how sex differences are represented in biventricular models derived from cine cardiovascular magnetic resonance imaging.
Time-resolved biventricular meshes were reconstructed from 372 asymptomatic adults. Principal component analysis was applied separately to end-diastolic mesh coordinates, representing anatomy, and to full-cycle end-diastolic-referenced Lagrangian displacement fields, representing function. Pooled and sex-specific PCA spaces were compared using variance partitioning, mode alignment, and bootstrap stability analysis.
Four anatomical modes satisfied bootstrap stability criteria. The leading pooled anatomical mode explained 31% of total shape variance and was dominated by between-sex differences, which accounted for 57% of that mode's variance. In contrast, five stable functional modes explained 67% of displacement variance and remained closely aligned between pooled and sex-specific decompositions.
These findings show that sex-related differences are represented differently in anatomical and functional PCA models: between-sex variation dominated the leading anatomical mode, whereas dominant functional displacement modes remained closely aligned between sexes. This suggests that, despite large sex-specific anatomical differences, the principal functional patterns captured by the model are largely preserved between sexes in asymptomatic adults.

Keywords: cardiac digital twins, sex-stratification, spatiotemporal modelling, statistical shape models.

1 Introduction

Cardiac digital twins derived from medical imaging aim to provide patient-specific representations of cardiac anatomy and function that can support phenotyping, simulation, and clinical decision support [1, 2]. However, for interpretation and statistical analysis,

these high-dimensional representations are usually reduced to lower-dimensional descriptors. Linear models, particularly principal component analysis (PCA), are commonly used for this purpose because they provide ordered and directly visualizable modes of population variation [3-5]

For anatomical descriptions, usually at end-diastole or end-systole, these low-dimensional representations have shown to contain information beyond standard scalar biomarkers such as volume, mass, ejection fraction, and sphericity [6] [7, 8] and are strongly associated with age, sex, cardiovascular risk factors, and disease status [9-11]. However, when male and female participants are modelled in a single pooled PCA space, the leading anatomical modes may reflect global scale and sex-related morphology rather than within-sex variation [12-14]. This is highly relevant for digital-twin construction, because the reference space used to parameterize anatomy determines which sources of variation are represented as dominant and which are relegated to lower-order components.

While digital twins have predominantly focused on these static morphological features, true cardiac function depends on the full-cycle dynamic motion of the myocardium and valves [15-18]. Effectively capturing this behaviour requires high-fidelity spatiotemporal models [16, 19]. However, it remains unclear whether sex stratification is equally critical for these functional latent spaces, or whether functional displacement models instead capture dominant, fundamental motion patterns that are fundamentally shared across males and females.

In this study, we investigated sex stratification in PCA-based biventricular digital-twin representations derived from cine CMR. High-fidelity, time-resolved biventricular meshes were reconstructed in 372 asymptomatic adults. We considered pooled PCA spaces for both end-diastolic anatomy and full-cycle Lagrangian displacement fields. These anatomical and functional representations were rigorously evaluated using variance partitioning, mode alignment and bootstrap stability.

2 Method

2.1 Dataset

The analysis used data from the SwissHeart cohort, a cross-sectional CMR study of asymptomatic adults aged 18 to 85 years, approved by the Ethics Committee of the Canton of Zurich with written informed consent from all participants. Imaging was performed at 1.5T Philips scanner and included bSSFP cine acquisitions in short-axis and long-axis views, (spatial resolution 1.0×1.0 mm^2, 8 mm slice thickness), together with a late-diastolic respiratory-gated 3D thorax scan used for spatial registration (spatial resolution of 0.8x0.8x0.8mm^3).

Participants were restricted to Caucasian/White volunteers without manifested cardiovascular disease, including prior myocardial infarction, coronary artery disease, arrhythmia, myocardial hypertrophy, aortic dissection, aortic valve stenosis, cardiomyopathy, atrial fibrillation, valve regurgitation, or hypertension. Of 382 eligible participants, 10 were excluded because of failure of automated segmentation or mesh-fitting,

resulting in 372 analysed subjects, 185 males and 187 females. Demographic, anthropometric, and haemodynamic characteristics are summarized in Table 1.

2.2 CMR segmentation and biventricular mesh reconstruction

Cine CMR images were segmented automatically using publicly available nnU-Net models trained on UK Biobank cardiac data[2]. Short-axis segmentations were used to extract ventricular endocardial and epicardial contours, while long-axis views were used to identify valve-plane and aortic-root landmarks.

Contours and landmarks were transformed into a common patient coordinate system. Breath-hold-related slice offsets were corrected using the respiratory-gated 3D thorax acquisition as an anatomical reference. A biventricular template mesh was then initialised for each subject using landmark-based rigid alignment and least-squares optimisation. Non-rigid fitting was performed with hierarchical free-form deformation over the full cardiac cycle, with temporal regularisation to obtain smooth time-resolved meshes with consistent point correspondence across subjects and phases [19]. Method verification included comparison of automated segmentations with expert manual contours and comparison of mesh-derived ventricular volumes with segmentation-derived volumes across the cohort.

Conventional imaging biomarkers were computed from the fitted time-resolved meshes to support cohort characterization and mode interpretation. Peak strains were computed from the anatomical average of Lagrangian strains projected in the radial, circumferential and longitudinal directions.

2.3 Anatomical and functional models

Before PCA, all meshes were rigidly aligned into a common anatomical frame using the LV apex and mitral, tricuspid, and aortic valve landmarks [20]. No isotropic scaling was applied, so absolute cardiac size remained part of the representation.

The anatomical model was constructed from end-diastolic meshes by concatenating aligned vertex coordinates into subject-level shape vectors. PCA was then applied to derive biventricular anatomical modes. A volume-weighted PCA formulation was evaluated but did not materially change the modes, so standard PCA was retained.

The functional model was constructed from end-diastolic-referenced Lagrangian displacement fields. For each cardiac phase, vertex-wise displacement was computed relative to the subject's aligned end-diastolic mesh. This separated baseline anatomy from within-cycle motion, unlike direct PCA of time-resolved coordinates where anatomy and deformation are mixed [21].

Displacement sequences were temporally normalized prior to PCA because to account for inter-subject variability in the number of cine frames. End-systole was identified from the time point of minimum LV volume [22], and systolic and diastolic segments were resampled separately, following prior cardiac motion-atlas and spatiotemporal mapping approaches [16, 23, 24], to account for the different scaling of the two phases with heart rate variations. Each sequence was resampled to 40 frames, 13 systolic and 27 diastolic phases, concatenated across space and time, and used for functional PCA.

2.4 PCA stability analysis

PCA modes were evaluated for reproducibility before being used as digital-twin descriptors. PCA was first computed on the full cohort to obtain a reference set of modes truncated to explain more than 95% of variance [1]. Because neighbouring eigenvalues can lead to mode mixing, the set was partitioned into blocks using relative eigenvalue gaps [25-27]. Spectral-gap significance was assessed with a permutation-based null model and Bonferroni correction [27-29].

The cohort was split into training and held-out subsets. Bootstrap resampling was performed on the training set, PCA was recomputed for each bootstrap sample, and bases were aligned to the reference basis using block-wise orthogonal Procrustes alignment. Subspace stability was quantified using principal angles from held-out score correlations. Modes were retained only when the median spectral angle was below 25°.

Pooled PCA models were computed for anatomy and function, and we assessed explained variance, mode interpretation and sex-wise variance partitioning.

3 Results

3.1 Cohort and mesh reconstruction

The final cohort included 372 asymptomatic participants, 185 males and 187 females. Males had larger body size, ventricular volumes, and LV myocardial mass than females, while ejection fractions and strains were higher in females (Table 1). The automated segmentation and mesh-fitting pipeline succeeded in 372 of 382 eligible subjects, corresponding to 97.4%. Short-axis Dice scores against manual contours were 0.95 (0.03) for LV blood pool, 0.90 (0.04) for RV blood pool, and 0.82 (0.05) for LV myocardium. On the full cohort, mesh-derived volumes closely matched estimates from segmentations, with errors of 7 (16) mL and 17 (18) mL for LVEDV and LVESV, and −12 (12) mL and −9 (18) mL for the corresponding RV volumes.

3.2 Stable anatomical and functional modes

PCA stability analysis identified four stable anatomical modes (PC_A) and five stable functional modes (PC_F) (Figure 1). The anatomical modes explained 61% of end-diastolic biventricular shape variance and showed reproducible bootstrap structure, with mean principal angles between 7° and 19°. The five functional modes explained 67% of full-cycle displacement variance and showed mean principal angles between 7° and 20°. Modes beyond the retained sets showed lower reproducibility and were excluded from the descriptor set.

Table 1. Sex-specific demographic, volumetric and functional characteristics of the volunteers included in this study. Values are reported as mean (standard deviation). Abbreviations: BSA, body-surface area ratio, LVEDV/LVESV, left ventricular end-diastolic/end-systolic volume; LVEF/RVEF, left/right ventricular ejection fraction; LVSV/RVSV, left/right ventricular stroke volume; LVM, left ventricular mass; Ψ_{ED}/Ψ_{ES}, sphericity index at end-diastole/end-systole; GRS/GCS/GLS, global radial/circumferential/longitudinal strain; E', early diastolic mitral annular velocity; S', systolic mitral annular velocity; V_c / V_r, EDV-normalised peak contraction/relaxation velocity; MAPSE/TAPSE, mitral/tricuspid annular plane systolic excursion.

	Male	Females		Male	Females
N, -	185	187	**SBP, mmHg**	130 (14)	118 (13)
Age, years	42 (14)	43 (14)	**DPB, mmHg**	78 (10)	77 (9)
Weight, kg	81 (12)	64 (8)	**HR, bpm**	66 (11)	70 (11)
Height, cm	181 (7)	167 (6)	**BSA, m²**	2.01 (0.17)	1.72 (0.12)
LVEDV, mL	145 (23)	105 (17)	**RVEDV, mL**	145 (26)	100 (19)
LVESV, mL	58 (13)	38 (8)	**RVESV, mL**	59 (15)	36 (10)
LVEF, -	60 (5)	63 (4)	**RVEF, -**	60 (6)	64 (5)
LVM, g	118 (20)	79 (13)			
Ψ_{ED}, -	0.25 (0.04)	0.24 (0.05)	**Ψ_{ES}, -**	0.19 (0.04)	0.19 (0.04)
MAPSE, mm	24 (3)	24 (3)	**E', cm/s**	15 (1.5)	13 (1.7)
TAPSE, mm	28 (4)	29 (3)	**S', cm/s**	-12 (2.4)	-7 (2.4)
V_c, EDV/S	-2.8 (0.4)	-2.8 (0.5)	**V_r, EDV/S**	2.6 (0.6)	2.7 (0.6)
GRS, -	0.50 (0.10)	0.52 (0.11)	**GCS, -**	-0.15 (0.02)	-0.16 (0.02)
GLS, -	-0.19 (0.04)	-0.20 (0.04)			

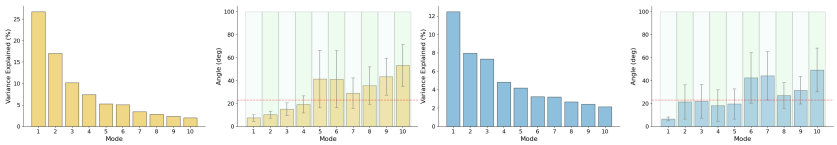

Figure 1. Stability analysis of anatomical (yellow) and functional (blue) PCA modes. For each case, left variance explained per mode. Right: distribution of principal angles, with green and white regions indicating the identified spectral blocks.

3.3 Interpretation of anatomical modes

The four stable pooled anatomical modes described distinct components of end-diastolic biventricular shapes (Figure 2). The first mode was dominated by scaling. A perturbation from negative to positive scores (±4 standard deviations of the scores range) produced changes of 91.2% in LV blood-pool volume, 97.9% in RV blood-pool volume, and 96.0% in LV myocardial volume, with a 28.9% change in average LV wall thickness. This mode therefore represented global cardiac size and myocardial mass.

The remaining stable anatomical modes were less volume-dominated and more geometric. Across modes 2 to 4, LV blood-pool volume changed by only 2.6% to 4.2%, RV blood-pool volume by 0.7% to 5.8%, LV myocardial volume by 0.4% to 4.8%, and average wall thickness by 3.5% to 4.3%. These modes represented sphericity, wall-thickness-related variation, valve-plane orientation, LV/RV volume balance, and LV-RV junction geometry. Thus, the pooled anatomical PCA space was concentrated around a dominant size-related first mode followed by smaller geometric modes.

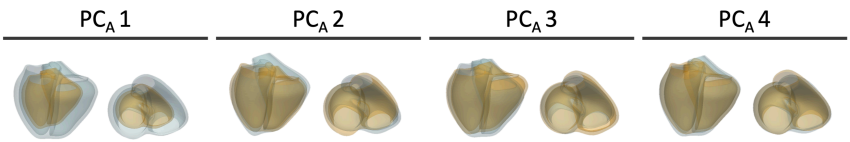

Figure 2. Leading anatomical modes. Shape variations are shown at ±2 standard deviations of each anatomical score, with negative and positive deviations displayed in light orange and light blue, respectively. Green boxes indicate the modes identified as stable.

3.4 Interpretation of functional modes

The first functional mode was dominated by longitudinal systolic motion and biventricular emptying. Perturbation along this mode changed MAPSE by 27.7%, TAPSE by 30.9%, LVESV by 14.4%, RVESV by 27.7%, LVEF by 5.6%, and RVEF by 11.5%. It therefore represented the main amplitude axis of systolic longitudinal function and global biventricular emptying.

Modes 2 and 3 captured relaxation-dominant patterns, with their largest effects on early-diastolic annular motion and peak relaxation velocity, and smaller effects on ejection fraction. Mode 4 and 5 had minor impact on functional indices. Overall, the functional modes represented longitudinal contraction, relaxation dynamics, annular motion, and biventricular volume change rather than static cardiac size.

3.5 Sex effects in anatomical and functional models

The anatomical PCA model showed strong sex-related structure in its leading component. The first pooled anatomical mode explained 31% of total anatomical variance, compared with 22% and 19% for the first male-specific and female-specific modes. Variance partitioning showed that 57% of the leading pooled mode variance was attributable to between-sex differences, while 26% and 17% reflected within-male and within-female variation. Subsequent pooled anatomical modes showed minimal between-sex contribution and were dominated by within-sex variation.

Functional displacement PCA showed the opposite pattern. The retained pooled functional modes were dominated by within-sex variation, with only small between-sex contributions. Similar variances and mean values were observed for both male, and females, suggesting closer alignment of male and female patterns to those of the anatomical model.

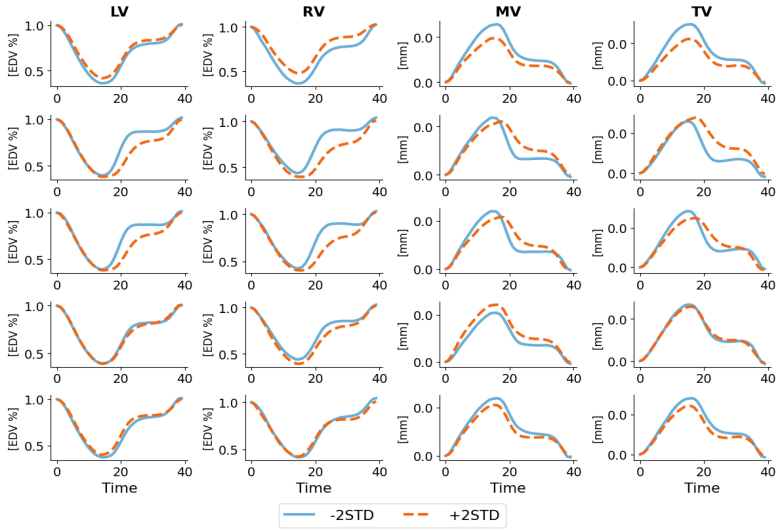

Figure 3. Global functional variations encoded by the stable functional. Cardiac displacements over the cardiac cycle are reconstructed by perturbing the mean pattern by ±2 standard deviations along each mode (solid and dashed lines, respectively) and added to the mean ED reference shape. For each reconstructed deformation, left and right ventricular volumes and mitral and tricuspid annular displacements are computed. Volumes are normalized by the initial LVEDV. Each row corresponds to a a mode from 1 (top) to 5 (bottom).

4 Discussion

This study tested whether sex stratification has the same relevance for PCA-based anatomical and functional representations in CMR-derived biventricular digital twins. Sex-related variation dominated the anatomical space but not the leading functional displacement space. In the pooled anatomical model, the first mode explained 31% of anatomical variance, 57% of which reflected between-sex differences. Thus, the pooled anatomical model efficiently described population variance, but its leading coordinate was strongly influenced by sex-related morphology.

The functional displacement model behaved differently. Five stable modes explained 67% of full-cycle displacement variance and represented longitudinal contraction, biventricular emptying, relaxation dynamics, and annular motion. These modes were dominated by within-sex variation and remained closely aligned between pooled and sex-specific decompositions. Therefore, in this asymptomatic cohort, a shared functional space preserved the dominant biventricular motion patterns without being primarily organized by sex.

5 Limitations

This study has several limitations. First, the cohort was cross-sectional, so age associations describe between-subject differences rather than longitudinal remodelling. Second, the analysis was restricted to asymptomatic Caucasian/White adults from a single-centre Swiss cohort, limiting generalizability to other populations, scanner protocols, and disease groups. Third, the results depend on automated segmentation and mesh fitting. Although method verification showed good segmentation accuracy and volume agreement, residual reconstruction errors may affect local anatomical or motion features. Fourth, the analysis was limited to linear PCA models. Nonlinear models may organize sex, anatomy, and function differently. Finally, sex-specific PCA reduces sample size, and larger cohorts may reveal additional stable higher-order modes. In addition, this conclusion is specific to linear PCA models and should not be assumed to generalize to nonlinear latent representations without validation.

6 Conclusions

In PCA-based CMR-derived biventricular digital-twin representations, sex stratfication had different relevance for anatomy and function. The leading pooled anatomical mode was dominated by between-sex morphology and global cardiac scale. In contrast, despite significant differences between males and females, dominant functional displacement modes were stable, mainly driven by within-sex variation, and closely aligned.

Disclosure of Interests. The authors have no competing interests to declare that are relevant to the content of this article.

References

1. Buoso, S., T. Joyce, and S. Kozerke, *Personalising left-ventricular biophysical models of the heart using parametric physics-informed neural networks.* Med Image Anal, 2021. **71**: p. 102066.
2. Ugurlu, D., et al., *Cardiac digital twins at scale from MRI: Open tools and representative models from ~ 55000 UK Biobank participants.* PLoS One, 2025. **20**(7): p. e0327158.
3. Zhang, X., et al., *Atlas-based quantification of cardiac remodeling due to myocardial infarction.* PLoS One, 2014. **9**(10): p. e110243.
4. Bai, W., et al., *A bi-ventricular cardiac atlas built from 1000+ high resolution MR images of healthy subjects and an analysis of shape and motion.* Med Image Anal, 2015. **26**(1): p. 133–45.
5. Beetz, M., et al., *Interpretable cardiac anatomy modeling using variational mesh autoencoders.* Front Cardiovasc Med, 2022. **9**: p. 983868.
6. Stokke, T.M., et al., *Geometry as a Confounder When Assessing Ventricular Systolic Function: Comparison Between Ejection Fraction and Strain.* J Am Coll Cardiol, 2017. **70**(8): p. 942–954.
7. Corral Acero, J., et al., *Understanding and Improving Risk Assessment After Myocardial Infarction Using Automated Left Ventricular Shape Analysis.* JACC Cardiovasc Imaging, 2022. **15**(9): p. 1563–1574.
8. Pizarro, G. and B. Ibanez, *Post-Myocardial Infarction Risk Prediction: Does Ventricular Shape Matter?* JACC Cardiovasc Imaging, 2022. **15**(9): p. 1575–1577.
9. Mauger, C.A., et al., *Longitudinal trajectories of left ventricular myocardial remodeling: associations with cardiovascular risk factors in the multi-ethnic study of atherosclerosis.* J Cardiovasc Magn Reson, 2025. **27**(2): p. 101943.
10. Burns, R., et al., *Relationships between heart shape, function, and disease in 38,858 UK biobank participants.* J Cardiovasc Magn Reson, 2025. **27**(2): p. 101919.
11. Buoso, S., et al., *MRXCAT2.0: Synthesis of realistic numerical phantoms by combining left-ventricular shape learning, biophysical simulations and tissue texture generation.* J Cardiovasc Magn Reson, 2023. **25**(1): p. 25.
12. Moscoloni, B., et al., *Unveiling sex dimorphism in the healthy cardiac anatomy: Fundamental differences between male and female heart shapes.* J Physiol, 2025.
13. Raisi-Estabragh, Z., et al., *Cardiovascular Magnetic Resonance Reference Ranges From the Healthy Hearts Consortium.* JACC Cardiovasc Imaging, 2024. **17**(7): p. 746–762.
14. Petersen, S.E., et al., *Reference ranges for cardiac structure and function using cardiovascular magnetic resonance (CMR) in Caucasians from the UK Biobank population cohort.* J Cardiovasc Magn Reson, 2017. **19**(1): p. 18.
15. Adams, J., et al., *Learning spatiotemporal statistical shape models for non-linear dynamic anatomies.* Front Bioeng Biotechnol, 2023. **11**: p. 1086234.
16. Puyol-Anton, E., et al., *A multimodal spatiotemporal cardiac motion atlas from MR and ultrasound data.* Med Image Anal, 2017. **40**: p. 96–110.
17. Bello, G.A., et al., *Deep learning cardiac motion analysis for human survival prediction.* Nat Mach Intell, 2019. **1**: p. 95–104.

18. Xia, Y., et al., *Automatic 3D+t four-chamber CMR quantification of the UK biobank: integrating imaging and non-imaging data priors at scale.* Med Image Anal, 2022. **80**: p. 102498.
19. Joyce, T., et al., *Rapid inference of personalised left-ventricular meshes by deformation-based differentiable mesh voxelization.* Med Image Anal, 2022. **79**: p. 102445.
20. Kabsch, W., *A solution for the best rotation to relate two sets of vectors.* Acta Crystallographica Section A, 1976. **32**(5): p. 922–923.
21. Ma, Q., et al., *Learning a dynamic four-chamber shape model of the human heart for 95,695 UK Biobank participants.* 2026. **arXiv 2603.28711**.
22. Schulz-Menger, J., et al., *Standardized image interpretation and post-processing in cardiovascular magnetic resonance-2020 update Society for Cardiovascular Magnetic Resonance (SCMR): Board of Trustees Task Force on Standardized Post-Processing.* Journal of Cardiovascular Magnetic Resonance, 2020. **22**(1).
23. Zhao, D., et al., *Correcting bias in cardiac geometries derived from multimodal images using spatiotemporal mapping.* Sci Rep, 2023. **13**(1): p. 8118.
24. Chung, C.S., M. Karamanoglu, and S.J. Kovacs, *Duration of diastole and its phases as a function of heart rate during supine bicycle exercise.* Am J Physiol Heart Circ Physiol, 2004. **287**(5): p. H2003–8.
25. Liu, X.F., et al., *Affinity matrix with large eigenvalue gap for graph-based subspace clustering and semi-supervised classification.* Engineering Applications of Artificial Intelligence, 2020. **93**.
26. Davis, C. and W.M. Kahanm, *The rotation of Eigenvectors by a perturbation.* SIAM Journal on Numerical Analysis, 1970. **7**.
27. Ogita, T. and K. Aishima, *Iterative refinement for symmetric eigenvalue decomposition II: clustered eigenvalues.* Japan Journal of Industrial and Applied Mathematics, 2019. **36**(2): p. 435–459.
28. Josse, J. and F. Husson, *Selecting the number of components in principal component analysis using cross-validation approximations.* Computational Statistics & Data Analysis, 2012. **56**(6): p. 1869–1879.
29. Johnstone, I.M., *On the distribution of the largest eigenvalue in principal components analysis.* Annals of Statistics, 2001. **29**(2): p. 295–327.